NURBS plasticity: yield surface evolution and implicit stress integration for isotropic hardening

William M. Coombs[a], Yousef Ghaffari Motlagh[b]

[a]*School of Engineering and Computing Sciences, Durham University*
Science Site, South Road, Durham, DH1 3LE, UK.
T: +44 (0) 191 334 2516, F: +44 (0) 191 334 2408, E: w.m.coombs@durham.ac.uk
[b]*School of Chemical and Process Engineering, University of Leeds, Leeds LS2 9JT, UK.*

Abstract

This paper extends the non-uniform rational basis spline (NURBS) plasticity framework of Coombs et al. [8] to include isotropic hardening of the yield surfaces. The approach allows any smooth isotropic yield envelope to be represented by a NURBS surface. The key extension provided by this paper is that the yield surface can expand or contract through the movement of control points linked to the level of inelastic straining experienced by the material. The model is integrated using a fully implicit backward Euler algorithm that constrains the return path to the yield surface and allows the derivation of the algorithmic consistent tangent to ensure optimum convergence of the global equilibrium equations. This provides a powerful framework for elasto-plastic constitutive models where, unlike the majority of models presented in the literature, the underlying numerical algorithm (and implemented code) remains unchanged for different yield surfaces. The performance of the algorithm is demonstrated, and validated, using both material point and boundary values simulations including plane stress, plane strain and three-dimensional examples for different yield criteria.

Keywords:
elasto-plasticity, constitutive modelling, non-uniform rational basis spline (NURBS), stress integration, finite-element analysis, isotropic hardening

1. Introduction

Robust and efficient constitutive models are at the heart of every boundary value stress analysis problem, providing the essential link between stress and strain for the material that they represent. Elasto-plasticity is one class of inelastic material behaviour that allows these models to predict yield and capture post-yield behaviour. Central to these models is the concept of a yield surface that provides the boundary between elastic (inside the surface) and elasto-plastic behaviour (on the surface). However, such models are typically developed in rate form, providing a rate relationship between stress and stain that

conflicts with an incremental boundary value solver, such as the finite element method. These boundary value solvers work with finite steps of stress and strain and therefore the rate-form constitutive relationships must be integrated. Typically the form of the yield surface impacts on the stress integration algorithm which requires changes in the numerics for each implemented yield surface. This issue was overcome by the paper of Coombs et al. [8] for yield surfaces that are fixed in stress space, known as perfect plasticity. It allowed any smooth isotropic yield surface to be modelled without changing the numerical algorithm or underlying code by using non-uniform rational basis spline (NURBS) surfaces to represent the yield envelope. This paper extends that work to allow for isotropic expansion/contraction of the yield surface.

In this paper we do not attempt to review the vast number of constitutive models and specific stress integration methods available in the literature and instead provide a simplistic overview of the different approaches. The works of Yu [33], Simo and Hughes [23] and Kojić [13] provide a review of constitutive models, detail stress integration approaches and provide strategies for implementation within finite element analysis, respectively.

The implementation of constitutive models at a material point level can be coarsely divided into three categories, namely: (i) explicit [12, 18, 20], (ii) implicit [9, 23, 32] and (iii) exact stress integration [14–17, 28, 29, 31]. Critically explicit approaches do not enforce the consistency conditions (see Section 2.1) at the updated stress state [30] and exact integration approaches are too computationally expensive for use in general finite element analysis [17].

Here we follow the approach of Coombs et al. [8] and adopt an implicit stress integration algorithm (elastic prediction followed by a plastic correction) coupled with an associated flow plasticity formulation that expresses the yield envelope as a NURBS surface. This allows any smooth isotropic yield function to be included within the same numerical framework. The key extension that we allow here is for the yield surface to expand (hardening) or contract (softening) under plastic straining. This is achieved by allowing the position of the control points to be a function of inelastic straining. This extends the NURBS plasticity framework to include materials where the yield stress is a function of the history of plastic straining that the body has experienced.

The layout of the paper is as follows, Section 2 provides the theoretical framework for hardening NURBS-based plasticity, including the definition of the NURBS surface, isotropic hardening through the movement of control points, the form of stress integration used and the technique of energy mapped stress that allows us to interpret the stress integration method as a geometric projection. Section 3 provides details on the numerical implementation including the backward Euler stress integration process and the algorithmic consistent tangent. Numerical examples are presented in Section 4 and, finally, conclusions are drawn in Section 5.

The majority of the paper is presented in tensor form using index notation, the notable exception is the numerics that are presented in matrix-vector form for ease of implementation. Consistent with the work of Coombs et al. [8], most of the paper is presented in

terms of principal stresses with a tension positive notation and the conventional ordering

$$\sigma_1 \geq \sigma_2 \geq \sigma_3.$$

Adopting a principal stress notation is common in other isotropic plasticity models, for example see the work of [2, 4–6] amongst others, and does not change the generality of the algorithm (it is suitable for 1D, 2D and 3D analysis). At the end of the stress integration process the generalised, 6-component, stress and strain quantities are recovered using the principal directions associated with the trial information (see Section 3.2.1 for details). In this paper the 6-component stress and strain quantities are denoted using $\hat{(\cdot)}$ when expressed in matrix/vector format.

2. Hardening NURBS plasticity

This section provides the essential equations required to define an isotropically hardening NURBS surface and include it within a plasticity framework. There is significant overlap between the theory presented here and that of Coombs et al. [8], however the repetition is retained for the sake of clarity and to provide a self-contained formulation. For details on NURBS-based surfaces see Piegl and Tiller [21] and Coombs et al. [8] for the particular case of perfect plasticity yield envelopes.

A general NURBS surface can be expressed as

$$S_k(\xi,\eta) = \sum_{i=0}^{n}\sum_{j=0}^{m} R_{i,j}(\xi,\eta)(C_k)_{i,j} \tag{1}$$

where k is the physical index and C_k are the control point positions. The NURBS basis functions, $R_{i,j}$, are given by

$$R_{i,j}(\xi,\eta) = \frac{N_{i,p}(\xi)N_{j,q}(\eta)w_{i,j}}{\sum_{k=0}^{n}\sum_{l=0}^{m} N_{k,p}(\xi)N_{l,q}(\eta)w_{k,l}} \tag{2}$$

where $N_{i,p}$ and $N_{j,q}$ are the p^{th} and q^{th}-degree B-spline basis functions, ξ and η are the local positions within the Knot vectors and $w_{i,j}$ are the weights associated with the control points. In the work of Coombs et al. [8] the control points were fixed, this paper removes that restriction.

2.1. NURBS-based yield envelopes

Within the framework of NURBS plasticity [8], the yield surface can be expressed as

$$f = \Big(\sigma_i - S_i(\xi,\eta,\varepsilon_i^{\mathrm{p}})\Big)(S_{,\sigma})_i = 0, \tag{3}$$

where $\varepsilon_i^{\mathrm{p}}$ is the principal plastic strain state and σ_i the principal stress state. $(S_{,\sigma})_i$ is the partial derivative of (1) with respect to stress which is the same as the outward normal to the surface. This can be obtained through the cross product of the two local derivatives

$$(S_{,\sigma})_i = (S_{,\eta} \times S_{,\xi})_i = \epsilon_{ijk}(S_{,\eta})_j(S_{,\xi})_k, \tag{4}$$

where ϵ_{ijk} is the Levi-Civita tensor[1]. Using the assumption of associated plasticity this direction also provides the flow rule, that is the plastic strains evolve according to

$$\dot{\varepsilon}_i^{\mathrm{p}} = \dot{\gamma}(S_{,\sigma})_i, \tag{5}$$

where $\dot{\gamma}$ is the scalar plastic multiplier which must satisfy the Kuhn-Tucker-Karush consistency conditions

$$f(\sigma_i, \varepsilon_i^{\mathrm{p}}) \leq 0, \qquad \dot{\gamma} \geq 0 \qquad \text{and} \qquad f(\sigma_i, \varepsilon_i^{\mathrm{p}})\dot{\gamma} = 0. \tag{6}$$

These enforce the condition that the material must either be inside the yield surface with no inelastic straining ($f \leq 0$ and $\dot{\gamma} = 0$) or on the yield surface undergoing elasto-plastic deformation ($f = 0$ and $\dot{\gamma} \geq 0$).

2.2. Isotropic hardening

Introducing hardening into the NURBS yield surfaces results in a yield surface that is dependent on the level of inelastic straining at a material point, such as

$$C_k = h(\varepsilon_i^{\mathrm{p}})C_k^0, \tag{7}$$

where C_k and C_k^0 are the updated and the original control point positions and $h(\varepsilon_i^{\mathrm{p}})$ controls the evolution of the control points. For linear isotropic hardening we can assume

$$h(\varepsilon_i^{\mathrm{p}}) = 1 + \alpha||\int_0^t \dot{\varepsilon}_i^{\mathrm{p}} dt||, \tag{8}$$

where α is a material constant controlling the hardening ($\alpha > 0$) or softening ($\alpha < 0$) rate and perfect plasticity is obtained with $\alpha = 0$. We can approximate the isotropic hardening function to provide an incremental function of the form

$$h(\Delta\varepsilon_i^{\mathrm{p}}) = h_n + \alpha||\Delta\varepsilon_i^{\mathrm{p}}||, \tag{9}$$

where $h_n = h\big((\varepsilon_n^{\mathrm{p}})_i\big)$ is the value of the hardening function from the previously converged state and it is assumed that initially, $h_0 = 1$.

[1] $\epsilon_{ijk} = 0$ if $i = j$, $j = k$ or $k = i$, $\epsilon_{ijk} = 1$ for even permutations of i, j and k and $\epsilon_{ijk} = -1$ for odd permutations of i, j and k.

2.3. Stress integration & energy-mapped stress space

In this paper we adopt an implicit stress integration scheme that makes an initial estimate (or trial) for the stress state and then corrects it back onto the yield surface if it violates the yield criterion. Central to this algorithm is the idea of an elastic trial stress

$$\sigma_i^t = D_{ij}^{\mathrm{e}}(\varepsilon_t^{\mathrm{e}})_j, \tag{10}$$

where $(\varepsilon_t^{\mathrm{e}})_j$ is the elastic trial strain and D_{ij}^{e} contains the principal components of the linear elastic stiffness matrix. The principal elastic trial strain is obtained from the eigenvalues of the generalised second order tensor form of the trial elastic strain

$$(\varepsilon_t^{\mathrm{e}})_{ij} = (\varepsilon_n^{\mathrm{e}})_{ij} + \Delta\varepsilon_{ij}, \tag{11}$$

where $(\varepsilon_n^{\mathrm{e}})_{ij}$ and $\Delta\varepsilon_{ij}$ are the elastic strains from the previously converged state and the strain increment from the current step. When the trial stress, (10), is located outside of the yield surface ($f > 0$) it must be corrected back onto the yield surface. The updated (or returned) stress can be expressed as

$$\sigma_i^r = \sigma_i^t - \Delta\sigma_i^{\mathrm{p}}, \qquad \text{where} \qquad \Delta\sigma_i^{\mathrm{p}} = D_{ij}^{\mathrm{e}}\Delta\varepsilon_j^{\mathrm{p}} \tag{12}$$

and $\Delta\epsilon_j^{\mathrm{p}}$ is the plastic strain increment determined from the incremental form of the flow rule at the updated stress state. Once the updated stress state has been obtained it is straightforward to obtain the updated elastic strain using

$$(\varepsilon_{n+1}^{\mathrm{e}})_i = C_{ij}^{\mathrm{e}}\sigma_j^r, \tag{13}$$

where C_{ij}^{e} is the elastic compliance matrix (the inverse of D_{ij}^{e}). The updated hardening parameter, h, can also be obtained using (9). The problem of finding the updated stress state (and other internal variables) is often solved using an iterative backward Euler (bE) algorithm and is referred to as a closest point projection (CPP) approach. However, referring to this process as a CPP is misleading as the return stress is not the geometrically closest point (except in the case when Poisson's ratio is equal to zero), but rather the return stress that minimises an energy norm over the return path [23].

Consistent with the work of Coombs et al. [8], this integration scheme is combined with energy-mapped stress space (EMSS) [10] to reduce the stress integration process to the problem of finding the geometrically closest point on the yield surface to the trial stress state. A stress state in EMSS, ς_i, can be obtained using the following transformation

$$\varsigma_i = T_{ij}\sigma_j \tag{14}$$

where, for isotropic linear elasticity, T_{ij} is solely a function of Poisson's ratio ν, with the

form [8]

$$T_{ij} = \left(\sqrt{1-2\nu} - \sqrt{1+\nu}\right)/3 + \delta_{ij}\sqrt{1-\nu}. \tag{15}$$

This mapping leads to a squashing of the yield surface in the hydrostatic direction and a stretching in the deviatoric direction (see the work of [4, 8, 10] for examples of the transformation for various yield surfaces).

Once obtained, the updated stress state in EMSS is simply transformed back into conventional principal stress space using the inverse mapping of T_{ij}.

3. Numerical implementation

Consistent with the perfect plasticity implementation of Coombs et al. [8], here we use a coarse initial subdivision algorithm to provide the initial starting point for a bE implicit stress integration process. In this paper we do not provided details of the subdivision algorithm, see [8] for details. The rest of this section is focused on the implicit stress integration algorithm and the derivation of the algorithmic consistent tangent. Within this algorithm the return stress state σ_i^r is replaced by the local positions within the Knot vectors, ξ and η as the primary unknowns in the CPP problem (in addition to the updated hardening parameter).

3.1. Implicit stress integration

In this paper we adopt an implicit stress integration algorithm formulated within energy mapped stress space with three unknowns

$$\{x\} = \{\xi \qquad \eta \qquad h\}^T \tag{16}$$

that must be found where the following residuals are satisfied

$$\{r\} = \left\{(\varsigma_i^t - \varsigma_i^n)(S_{,\xi})_i \qquad (\varsigma_i^t - \varsigma_i^n)(S_{,\eta})_i \qquad h - \tilde{h}\right\}^T = \{0\}. \tag{17}$$

The first two residuals ensure that the return path in EMSS is perpendicular to the yield surface and the third that the hardening function has reached a stationary value, where

$$\tilde{h} = h_n + \alpha||\Delta\varepsilon_i^{\mathrm{p}}|| \qquad \text{and} \qquad \Delta\varepsilon_i^{\mathrm{p}} = C_{ij}^{\mathrm{e}} T_{jl}^{-1}(\varsigma_l^t - \varsigma_l^n). \tag{18}$$

In the above equation $\Delta\sigma_i^{\mathrm{p}} = T_{jl}^{-1}(\varsigma_l^t - \varsigma_l^n)$ is the plastic stress increment over the stress return path. The unknowns are updated through a standard Newton process

$$\{\delta x^k\} = -\left[\frac{\partial r}{\partial x}\right]^{-1}\{r^{k-1}\} \qquad \text{and} \qquad \{x^k\} = \{x^{k-1}\} + \{\delta x^k\}, \tag{19}$$

where k denotes the Newton-Raphson iteration number. The derivatives required for the Jacobian matrix, $[\partial r/\partial x]$, are provided in Appendix B. The starting point on the yield surface, (ξ_0, η_0), for the NR algorithm is the output from the subdivision process of Coombs et al. [8] with $h = h_n$ (that is, the yield surface is frozen during the subdivision). As with the algorithm for perfect plasticity, the stress return path for NR procedure described in this paper starts and remains in the yield envelope and thereby satisfies the consistency conditions not only at the final state but also during the stress updating algorithm.

3.2. Algorithmic consistent tangent

Efficient implementation of the constitutive model in a boundary value simulation requires the derivation of the algorithmic tangent modulus to ensure asymptotic quadratic convergence of the global out of balance force residual [25]. Here, the tangent is first constructed in principal stress space and then transformed into six-component stress space using the eigenvectors associated with the trial elastic strain state (see Appendix A for details). Following the approach of [3] (see page 29 for the full derivation), we can linearise the constitutive model into the following form

$$\underbrace{\begin{bmatrix} [C^{\mathrm{e}}] + \Delta\gamma[S_{,\sigma\sigma}\,] & \Delta\gamma\{S_{,\sigma h}\,\} & \{S_{,\sigma}\,\} \\ -\{\Delta\tilde{h}_{,\sigma}\,\}^T & 1 - \Delta\tilde{h}_{,h} & -\Delta\tilde{h}_{,\Delta\gamma} \\ \{S_{,\sigma}\,\}^T & f_{,h} & 0 \end{bmatrix}}_{[A^{alg}]^{-1}} \begin{Bmatrix} \{d\sigma\} \\ dh \\ d\Delta\gamma \end{Bmatrix} = \begin{Bmatrix} \{d\varepsilon_t^{\mathrm{e}}\} \\ 0 \\ 0 \end{Bmatrix}, \tag{20}$$

where the derivatives are determined at the updated stress state on the new yield surface. $\tilde{h}$ is the hardening function, and in this case

$$\Delta\tilde{h} = \alpha||\Delta\varepsilon_i^{\mathrm{p}}||. \tag{21}$$

The second derivative of the NURBS surface with respect to stress is

$$\begin{aligned} (S_{,\sigma\sigma}\,)_{ij} \;=\; & \Big(\epsilon_{ikl}(S_{,\eta}\,)_k(S_{,\xi\xi}\,)_l + \epsilon_{ikl}(S_{,\eta\xi}\,)_k(S_{,\xi}\,)_l\Big)(\xi_{,\sigma}\,)_j + \\ & \Big(\epsilon_{ikl}(S_{,\eta}\,)_k(S_{,\xi\eta}\,)_l + \epsilon_{ikl}(S_{,\eta\eta}\,)_k(S_{,\xi}\,)_l\Big)(\eta_{,\sigma}\,)_j, \end{aligned} \tag{22}$$

where derivatives of the local Knot coordinates with respect to stress can be obtained from the inversion of the Jacobian matrix linking the local NURBS coordinates with the principal stress directions, that is

$$[J] = \left[\frac{\partial\sigma}{\partial\xi}\right] = \Big[(S_{,\xi}\,)_i \quad (S_{,\eta}\,)_i \quad (S_{,\sigma}\,)_i\Big]. \tag{23}$$

The normal to the NURBS surface, $(S_{,\sigma})_i$ provides the third direction, orthogonal to the tangent vectors, in the transformation. The derivatives associated with the hardening function are

$$\{\Delta\tilde{h}_{,\sigma}\}^T = \alpha\frac{\{\Delta\varepsilon^{\rm p}\}^T}{||\Delta\varepsilon_i^{\rm p}||}\Delta\gamma[S_{,\sigma\sigma}], \tag{24}$$

$$\Delta\tilde{h}_{,h} = \alpha\frac{\{\Delta\varepsilon^{\rm p}\}^T}{||\Delta\varepsilon_i^{\rm p}||}\Delta\gamma\{S_{,\sigma h}\} \qquad \text{and} \tag{25}$$

$$\Delta\tilde{h}_{,\Delta\gamma} = \alpha\frac{\{\Delta\varepsilon^{\rm p}\}^T}{||\Delta\varepsilon_i^{\rm p}||}\{S_{,\sigma}\}. \tag{26}$$

The derivatives of the yield function and flow direction with respect to h are

$$f_{,h} = -\{S_{,h}\}^T\{S_{,\sigma}\} \qquad \text{and} \qquad \{S_{,\sigma h}\} = \{S_{,\sigma}\}h^{-1}. \tag{27}$$

Multiplying both sides of (20) by $[A^{alg}]$, allows us to obtain the principal components of the consistent tangent, $[D^{\rm alg}]$, as

$$\left\{\begin{array}{c}\{d\sigma\}\\ dh\\ d\Delta\gamma\end{array}\right\} = \left[\begin{array}{ccc}[D^{\rm alg}] & \{A_{12}^{alg}\} & \{A_{13}^{alg}\}\\ \{A_{21}^{alg}\}^T & A_{22}^{alg} & A_{23}^{alg}\\ \{A_{13}^{alg}\}^T & A_{32}^{alg} & A_{33}^{alg}\end{array}\right]\left\{\begin{array}{c}\{d\varepsilon_t^{\rm e}\}\\ 0\\ 0\end{array}\right\}, \tag{28}$$

where the transpose on the vector components denote row vectors and in this case there is symmetry between the 1-3 components of the matrix. $[D^{\rm alg}]$ provides the material tangent that is consistent with the constitutive model such that when it is used to construct the structural stiffness at a boundary value solver level we can obtain the optimum rate of convergence of the global equilibrium equations when solved with a Newton process.

3.2.1. Six-component stress space

Due to the geometric nature of this paper, the plasticity framework and stress integration process has been presented in principal stress space. Within this approach, and consistent with the approach of others [2, 4–6], we assume that the principal directions of the updated elastic strain state are coincident with the elastic trial state. This means that the principal directions do not change over the return path but they can changed between previous and updated stress state (see Coombs and Crouch [4] for more details on the consequence of crossing between sextants of stress space with implicit stress integration). However, in order to use the plasticity model in general analysis is it necessary to map between the principal and 6-component states and vice versa. This mapping is detailed in Appendix A for both stress/strain vectors and stiffness matrices. However, before we can map the material stiffness matrix it is necessary to specify its shear components in terms of the principal stresses.

The shear terms of the modified elastic stiffness matrix are given by

$$[D_G^c] = [A_G][D_G^e], \tag{29}$$

where $[D_G^e]$ is a three-by-three matrix containing the shear components of the 6-component elastic stiffness matrix. The modification matrix for the shear components is given by [2]

$$[A_G] = \begin{bmatrix} 1 + \frac{\Delta\sigma_1^p - \Delta\sigma_2^p}{\sigma_1^r - \sigma_2^r} & 0 & 0 \\ 0 & 1 + \frac{\Delta\sigma_1^p - \Delta\sigma_3^p}{\sigma_1^r - \sigma_3^r} & 0 \\ 0 & 0 & 1 + \frac{\Delta\sigma_2^p - \Delta\sigma_3^p}{\sigma_2^r - \sigma_3^r} \end{bmatrix}. \tag{30}$$

The stiffness matrix used in (A.1) is therefore

$$[D] = \begin{bmatrix} [D^{alg}] & [0] \\ [0] & [D_G^c] \end{bmatrix}, \tag{31}$$

where [0] is a three-by-three matrix full of zeros and $[D^{alg}]$ is the principal elastic stiffness matrix from (28). A pseudo-code for the isotropically hardening NURBS plasticity model is given in Figure 1 that details fully the steps required in calculating the updated stress state and hardening parameter.

4. Numerical simulations

This section provides material point and boundary value simulations to demonstrate the performance of the constitutive model and the numerical stress integration algorithm described in the previous sections.

4.1. Material point investigations

This set of numerical analyses considers an isotropically hardening von Mises yield envelope. The yield surface can be expressed as

$$f = \rho - h\rho_y = 0, \tag{32}$$

where the deviatoric stress is $\rho = \sqrt{2J_2}$ with $J_2 = \frac{1}{2}s_{ij}s_{ji}$ and $s_{ij} = \sigma_{ij} - \frac{1}{3}\sigma_{kk}\delta_{ij}$, ρ_y is the yield stress of the material and defines the radius of the von Mises cylinder. See Coombs et al. [8] for the Knot vectors and weights for the NURBS-based von Mises surface.

Figure 2 shows the convergence of the NR algorithm for a hardening von Mises yield surface with $E = 200$Pa, $\nu = 0.2$, $\rho_y = 1$Pa and $\alpha = 10$ subjected to a trial elastic strain of $\{\varepsilon_t^e\} = \{-10 \quad 4 \quad 5 \quad 0 \quad 0\}^T \times 10^{-3}$. The tolerance on the NR residual was set to 1×10^{-9} and two subdivisions were applied before starting the NR process. The initial hardening function, h_n, was set to unity and the converged value was $h = 1.055$.

1. INPUT: physical ($\{\varepsilon^t\}$, E, ν, h_n) & NURBS (Ξ, C_k, w, p) information.

   (a) Transform the trial elastic strain, $\{\varepsilon^t\}$, into its principal components and store the associated eigenvectors.

   (b) Calculate the principal (elastic) trial stress, $\{\sigma^t\} = [D^{\mathrm{e}}]\{\varepsilon^t\}$.

   (c) Calculate the current control point positions $[C_k]$ from (7) with $h = h_n$.

   (d) Transform the trial stress, $\{\sigma^t\}$, and the control point locations, $[C_k]$, to energy mapped stress space.

   (e) Determine the closest point between the trial stress state, $\{\varsigma^t\}$, and the hardening NURBS surface in energy mapped stress space, also obtaining h_{n+1}, based on the bE stress integration algorithm given in Section 3.1.

   (f) Determine the value of the yield function based on the the updated control points, the closest point and the trial state (3).

   (g) IF $f >$ tol (*elasto-plastic behaviour*)

      i. transform the return stress state, $\{\varsigma_{cp}\}$, back to conventional stress space;
      ii. calculate the updated elastic strain, $\{\varepsilon^{\mathrm{e}}_{n+1}\} = [D^{\mathrm{e}}]^{-1}\{\sigma_{n+1}\}$;
      iii. determine the algorithmic consistent tangent matrix, $[D^{a\,\mathrm{lg}}]$;

   (h) ELSE (*elastic behaviour*)

      i. updated stress equal to the trial stress, $\{\sigma_{n+1}\} = \{\sigma^t\}$;
      ii. updated elastic strain equal to the trial strain, $\{\varepsilon^{\mathrm{e}}_{n+1}\} = \{\varepsilon^t\}$; and
      iii. algorithmic tangent equal to the elastic tangent, $[D^{alg}] = [D^{\mathrm{e}}]$.
      iv. maintain the original hardening parameter, $h_{n+1} = h_n$.

   (i) END IF

   (j) Transform the principal components (updated stress, elastic strain and consistent tangent) back to generalised space using the eigenvectors stored at step (a) - see Appendix A.

2. OUTPUT: $\{\sigma_{n+1}\}$, $\{\varepsilon_{n+1}\}$, h_{n+1} and $[D^{alg}]$

Figure 1: Pseudo-code for the isotropically hardening NURBS constitutive model.

Figure 2 plots the current NR error, $||\{r_{n+1}\}||$, against both the iteration number and the residual from the previous iteration, $||\{r_{n+1}\}||$, the latter allows us to assess the convergence rate of the algorithm. The algorithm achieves a quadratic convergence rate on the final iteration demonstrating the correct implementation of the algorithm. The small inset figure in Figure 2 shows the trial and return stress states along with the final von Mises yield surface.

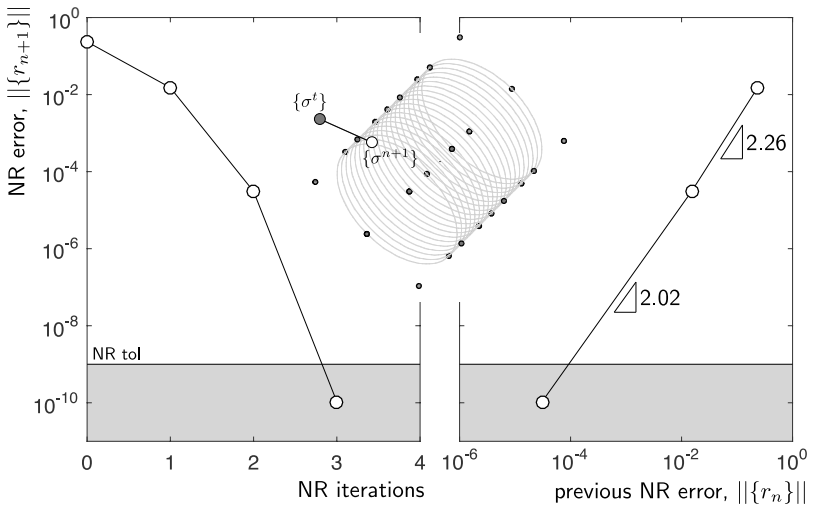

Figure 2: Convergence for a hardening von Mises yield surface with $E = 200$Pa, $\nu = 0.2$, $\rho_y = 1$Pa and $\alpha = 10$ subjected to a trial elastic strain of $\{\varepsilon_t^e\} = \{-10 \quad 4 \quad 5 \quad 0 \quad 0\}^T \times 10^{-3}$.

The stress integration errors for a von Mises yield surface (with the same material properties as above) using the NURBS integration procedure are shown in Figure 3. The stress state is initially located on the shear meridian in the $\sigma_{zz} > \sigma_{yy} > \sigma_{xx}$ sextant of stress space. This point is then subjected to a stress increment that will take the trial stress state outside of the yield envelope into one of the three sextants shown in Figure 3. The space of trial states was explored for $\rho_t/\rho_y \in [1, 6]$ and the errors associated with the trial state shown on the right of Figure 3. The normalised error measure used is

$$\text{error} = \frac{||\{\sigma_{\text{NURBS}}\} - \{\sigma_e\}||}{||\sigma_e||}, \tag{33}$$

where $\{\sigma_{\text{NURBS}}\}$ is the stress return location associated with the NURBS model and $\{\sigma_e\}$ is the exact stress return [14].

Although errors of over 20% are present in the model, exactly the same level of errors are observed in the von Mises yield surface integrated with a conventional bE stress integration procedure. As expected with any predictor-correction stress integration algorithm, the error increases as the tangential proportion of the stress increment increases. The errors

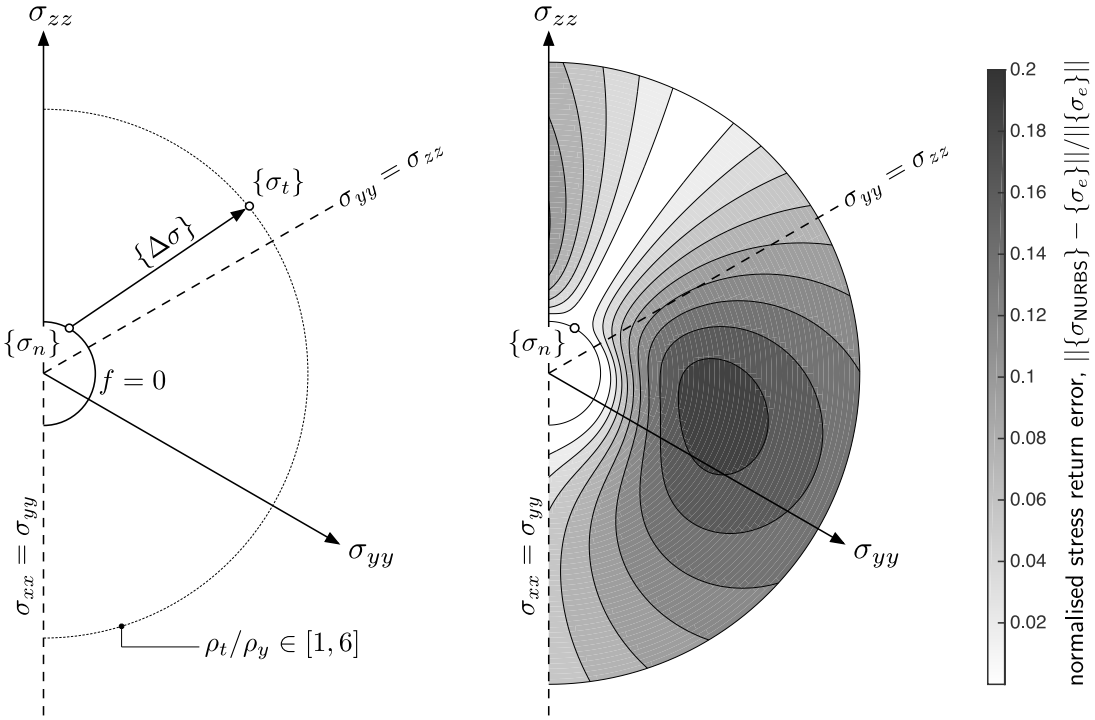

Figure 3: Stress return error analysis for an isotropically hardening von Mises NURBS yield envelope.

are almost identical to those reported by Coombs et al. [8] for the perfect plasticity yield surface and are consistent with the results shown by others using implicit stress integration [16]. Although these errors seem very large the analysis has explored a region of stress space up to 6 times the size of the yield envelope. Provided that sufficient loadsteps are adopted it is unlikely that a stress state would exceed the yield envelope by such a degree in a boundary value simulation and, as commented by Krieg and Krieg [16], these errors are unlikely to have a significantly detrimental impact. Despite this, the region of stress space explored indicates the stability of the proposed numerical framework.

Figure 4 (i) shows the converged hardening parameter value for the same range of trial stress states as analysed in Figure 3. As expected from (21), the value of the hardening parameter is only dependent on the magnitude of the plastic strain increment, or equivalently, the radial distance that the trial state is from the yield surface. Figure 4 (ii) gives the normalised error in the hardening parameter, the distribution of the error is similar to the stress errors shown in Figure 3 as the error in the stress increment will be proportional to the error in the return stress.

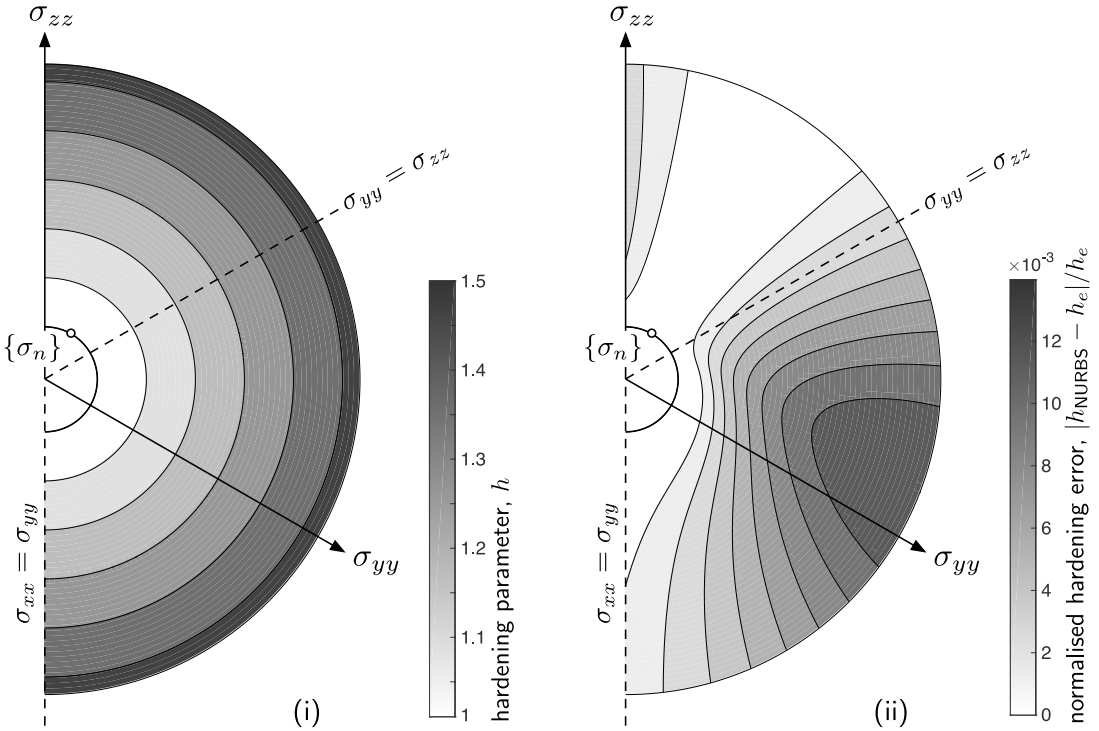

Figure 4: (i) stress return hardening parameter values and (ii) errors for an isotropically hardening von Mises NURBS yield envelope.

4.2. Boundary value simulations

This section presents the results from three boundary value simulations to demonstrate the performance of the proposed hardening NURBS framework. In all cases two subdivisions (see Coombs et al. [8] for details) were applied before initiating the backward Euler stress return algorithm.

4.2.1. Plane strain double notched plate

The first boundary value simulation presented in this paper is that of the plane strain stretching of a double-notched plate. The problem was initially presented by Nagtegaal et al. [19] and subsequently re-analysed in a number of papers, including [8, 22, 24, 26]. As shown in Figure 5, the plate was 30mm tall and 10mm wide with a 2mm unit linking ligament at mid height. The plate had a Young's modulus of 206.9GPa, Poisson's ratio of 0.29 and was modelled using an isotropically hardening von Mises yield surface with associated flow and an initial yield stress of $\rho_y = 0.45$GPa.

The analytical limit load for the case of perfect plasticity ($\alpha = 0$) is $f^{\text{lim}} \approx 2.673$kN [19]. Due to symmetry, only one quarter of the specimen was discretised, initially using 75 plane

strain eight-noded elements with reduced four-point integration. A displacement of 0.2mm was applied in to the top of the plate in 20 equal displacement-controlled increments.

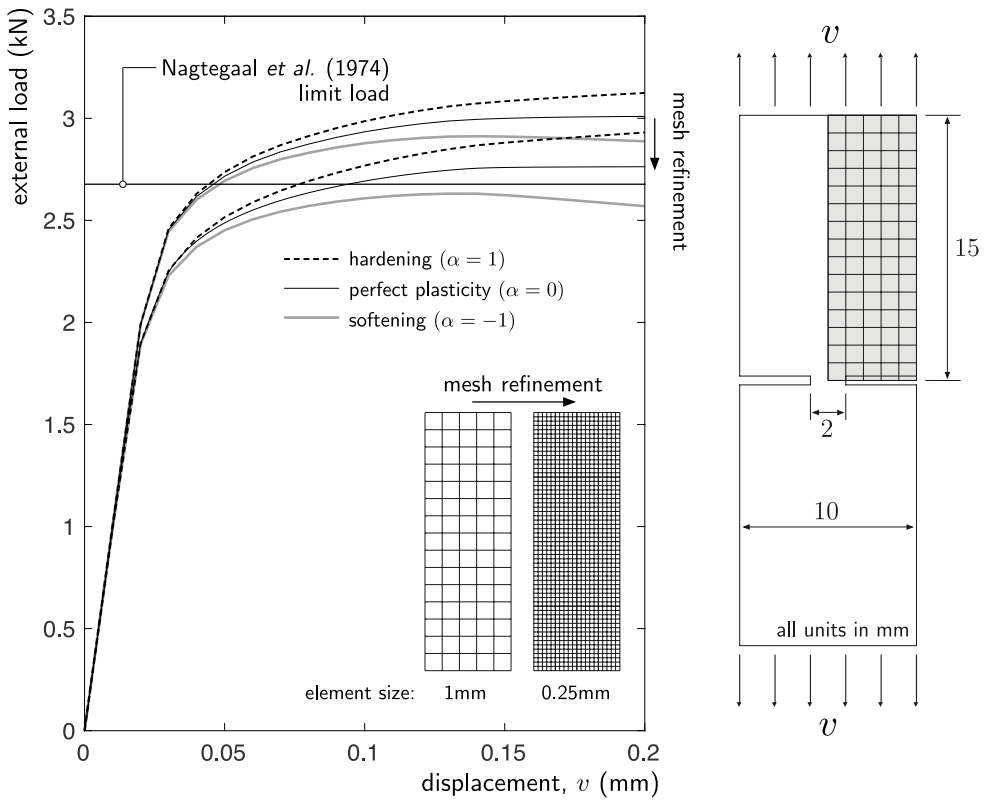

Figure 5: Double notched plate with NURBS-based von Mises plasticity with hardening, perfect plasticity and softening responses.

Figure 5 shows three different model responses for two finite element discretisations. The three cases are where $\alpha = 1$ (hardening or expansion of the yield surface, black dashed line), $\alpha = 0$ (perfect plasticity, fine black line) and $\alpha = -1$ (softening or contraction of the yield surface, thick grey line). As the mesh is refined the perfect plasticity response appears to approach the analytical limit load (refer to Coombs et al. [8] for a demonstration of this convergence over three meshes). As expected the hardening and softening responses predict force versus displacement responses above and below the perfect plasticity response, respectively.

The global normalised residual out of balance force

$$\bar{f}^{\text{oobf}} = \frac{||\{f^{\text{ext}}\} - \{f^{\text{int}}\}||}{||\{f^{\text{ext}}\}||}, \tag{34}$$

is given in Table 1 for each of the global Newton iterations for four loadsteps of the 75 element simulation with a softening yield surface with $\alpha = -1$. The tolerance on the residual was set to 1×10^{-8}. All of the loadsteps converged in five iterations, or fewer, with the final iterations within each loadstep approaching a quadratic convergence rate, demonstrating the correct implementation of the algorithmic consistent tangent for the constitutive model, including the case of material softening. For this case by the end of the simulation the minimum size of the yield surface had reduced to 78% of the original.

	loadstep			
NR iteration	2	3	10	20
1	8.953×10^{-2}	2.502×10^{-1}	2.392×10^{-2}	1.553×10^{-3}
2	6.891×10^{-3}	6.605×10^{-2}	9.518×10^{-4}	8.705×10^{-5}
3	4.050×10^{-5}	2.205×10^{-3}	1.278×10^{-6}	8.828×10^{-9}
4	1.435×10^{-9}	6.933×10^{-6}	1.270×10^{-12}	-
5	-	6.474×10^{-11}	-	-

Table 1: Plane strain notched plate convergence for the NURBS implementation of the von Mises yield surface with linear isotropic softening ($\alpha = -1$) with 75 elements (1×1mm element size).

4.2.2. Plane stress perforated plate

The next example is of the plane stress stretching of a perforated plate, as analysed by [23, 27], amongst others. Here the plane stress approach of de Borst [1] is implemented, such that the plane stress condition is enforced at the finite element level leaving the three dimensional constitutive model unchanged. The 1mm thick plate had a total width and height of 20mm and 36mm, respectively, and contained a 10mm hole at its centre, as shown in Figure 6. The material had a Young's modulus of 70GPa and a Poisson's ratio of 0.2. A von Mises yield surface was used with an initial yield radius of 0.198GPa and the hardening parameter was set to $\alpha = 0.82$ (note that here the yield stress a factor of $\sqrt{2/3}$ smaller than that used in [27] due to the difference in the von Mises yield criterion used in that work). Only one quarter of the plate was modelled due to the inherent symmetry in the problem and a displacement of 0.14mm was applied to the top edge of the plate over 7 equal loadsteps. The plate was initially discretised using 384 four-noded bi-linear quadrilateral elements integrated using 4-point Gaussian quadrature (note that volumetric locking is not an issue here due to the plane stress assumption in the third direction).

The left of Figure 6 compares the force versus displacement result of de Souza Neto et al. [27], shown by black squares, with the hardening NURBS model for two different meshes. The coarser mesh (384 elements, solid grey line) shows excellent agree with the result of [27] and there is little difference in the result when the mesh is refined to 768 elements (dashed black line). The right of Figure 6 (top left quarter of the plate) also

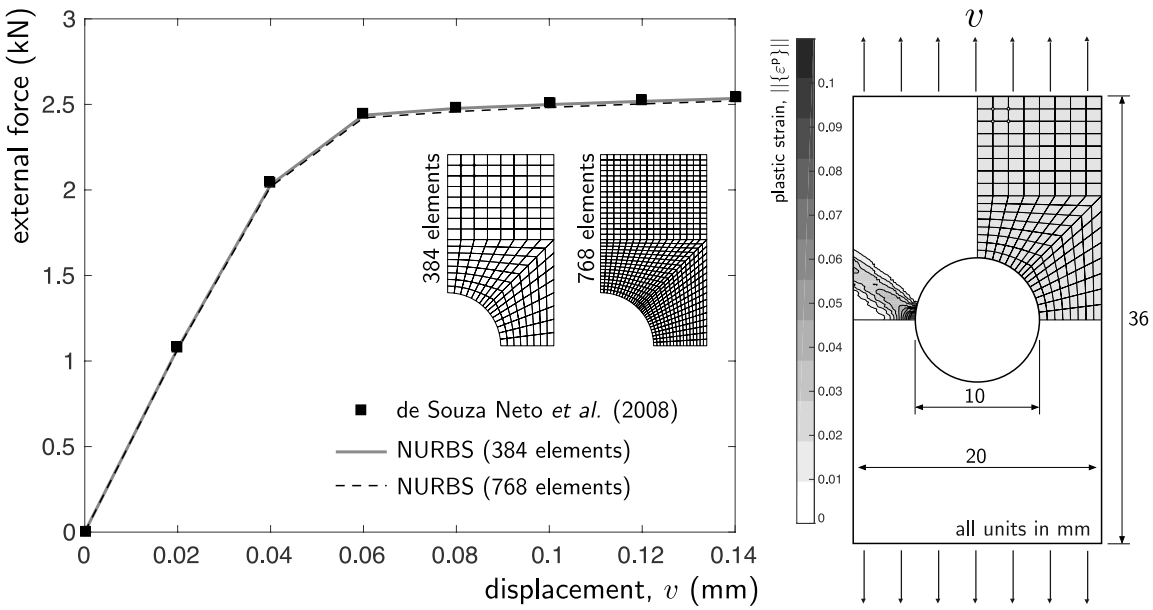

Figure 6: Plane stress perforated plate: comparison of the NURBS hardening von Mises model with the result of de Souza Neto et al. [27].

shows the accumulated plastic strain at the end of the simulation of the mesh with 768. This again shows good agreement with other results published in the literature [23, 27].

The global normalised residual out of balance force is given in Table 2 for each of the global Newton iterations for the final four loadsteps of the 384 element simulation. The tolerance on the residual was set to 1×10^{-8}. All of the loadsteps converged in five iterations, or less, with the final iterations within each loadstep approaching a quadratic convergence rate, demonstrating the correct implementation of both the algorithmic consistent tangent for the constitutive model and the consistency of the plane stress implementation.

	loadstep			
NR iteration	4	5	6	7
1	3.883×10^{-2}	3.433×10^{-2}	1.245×10^{-2}	7.405×10^{-3}
2	1.127×10^{-2}	3.520×10^{-3}	7.248×10^{-4}	8.531×10^{-4}
3	1.760×10^{-3}	1.120×10^{-4}	2.804×10^{-6}	3.699×10^{-6}
4	4.533×10^{-6}	1.113×10^{-7}	2.836×10^{-11}	9.444×10^{-11}
5	9.632×10^{-11}	1.049×10^{-13}	-	-

Table 2: Plane stress perforated plate convergence for the NURBS implementation of the von Mises yield surface with linear isotropic hardening with 384 elements.

4.2.3. Plane strain rigid footing

The penultimate example is that of a 1m wide plane strain rigid footing displacing into a weightless 10m by 5m domain with a Young's modulus of $E = 1 \times 10^7$kPa and a Poisson's ratio of $\nu = 0.48$. The yielding of the material was governed by a Drucker-Prager (D-P) yield envelope [11] with cohesion of $c = 490$kPa and a friction angle of $\theta = \pi/9$ (20 degrees).

The D-P yield envelope can be expressed as

$$f = \rho + \beta(\xi - \xi_a) = 0, \tag{35}$$

where $\xi = \sigma_{ii}/\sqrt{3}$, $\beta = \tan(\theta)$ is the opening angle of the cone and $\xi_a = c\sqrt{3}\cot(\phi)$ is the location of the cone's tensile apex. The tensile apex of the yield surface poses an issue for the stress return algorithm presented in this paper as the derivatives of the NURBS surface are undefined at this point. Here we follow the same approach as Coombs et al. [8] and locally round the apex, as shown in Figure 7 with $\xi_a = 0$. The yield surface is shown in both hydrostatic versus deviatoric stress space and principal stress space for both the original and rounded surfaces. The Knot vector and associated control point weights for the grey curve shown in Figure 7 (i) are

$$\Xi = \{0, 0, 0, 1, 1, 2, 2, 2\} \qquad \text{and} \qquad w = \{1, 1, 1, \cos(\phi/2), 1\}.$$

The radius of the rounding curve can be obtained from the hydrostatic position of the point where the true and rounded curves depart, point C in Figure 7 (i), that is

$$R = \xi_{\mathsf{C}} \frac{\tan(\theta)}{\cos(\theta)}, \qquad \text{where} \qquad \theta = \arctan(\beta),$$

$\xi_{\mathsf{C}} < \xi_a$ and the arc angle is $\phi = \pi/2 - \theta$. The hydrostatic locations of points D and E can be subsequently obtained from ξ_{C} and R, where point D lies on the intersection between the original yield curve and a line of constant hydrostatic pressure from the tensile limit of the rounded surface.

Without loss of generality in the level of error, we can consider the special case when the un-rounded yield surface is pinned at the hydrostatic axis (that is, $\xi_a = 0$) and the start of the rounding is expressed in terms of a deviation from the apex, $\xi_{\mathsf{C}} = \xi_a - \delta$. In this case the maximum hydrostatic error caused by the rounding can be expressed as

$$\text{error} = \delta \left(1 + \frac{\beta}{\cos(\theta)} \right). \tag{36}$$

For a given opening angle, β, the error varies linearly with δ that can be set based on the precision required.

The normalised pressure versus displacement results for the footing problem are shown

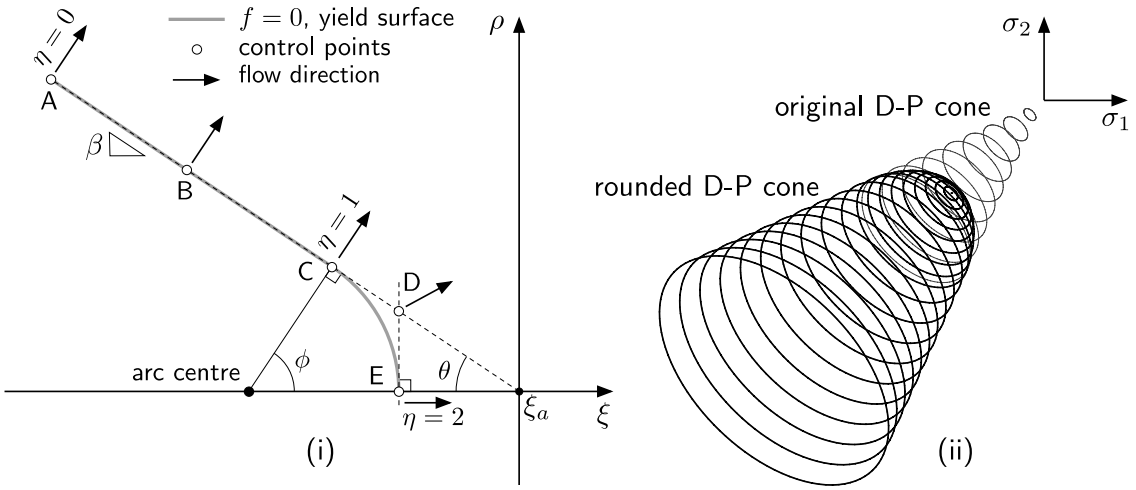

Figure 7: Drucker-Prager yield surface in: (i) hydrostatic, ξ, versus deviatoric, ρ, stress space and (ii) principal stress space showing both the rounded and original cones.

in Figure 8, where B is the footing width, p is the footing pressure and v is the vertical displacement of the footing. The problem was analysed using a mesh comprising 135 eight-noded bi-quadratic quadrilateral elements integrated using reduced four-point quadrature. Due to symmetry only half of the problem was modelled and the mesh detail around the corner of the footing is shown in the inset figure. The mesh is the same as that used by [4, 6–8, 27]. A vertical displacement of 4mm was applied to the footing over 20 equal loadsteps.

First we consider perfect plasticity ($\alpha = 0$) and validate the rounded D-P implementation. The solid grey line in Figure 8 shows the response of a conventional backward Euler implementation of the D-P perfect plasticity model that includes a tensile apex and the dashed black line the response of the rounded NURBS model for the case where $\delta = 1$MPa (note that the apex hydrostatic stress, ξ_a, is 2.33MPa for these material constants). The result from de Souza Neto et al. [27] is also shown by the discrete white squares. All three models show excellent agreement with the results being indistinguishable at the scale presented, with no stress states returning to the rounded part of the yield surface. The case of linear isotropic hardening is also presented with $\alpha = 100$ and the expected hardening response in the normalised pressure versus displacement behaviour is seen. At the end of the simulation there has been significant hardening in the model with a maximum value of h of 67.2.

4.2.4. Three-dimensional unit cube

The final example presented in this paper is that of a unit cube constrained with roller boundary conditions on three faces and subjected to two point loads on the unconstrained

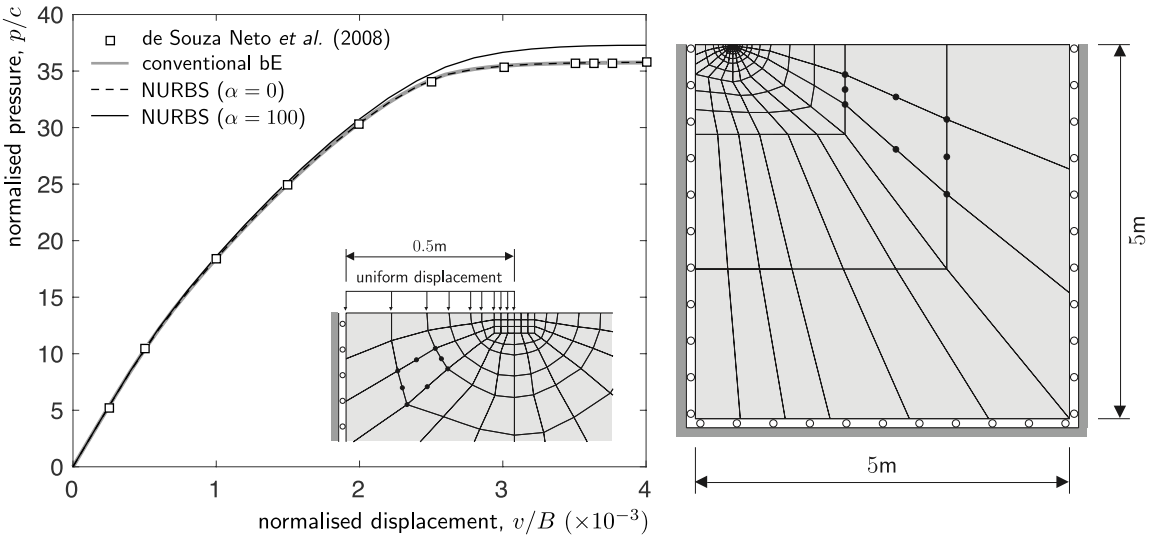

Figure 8: Plane strain footing analysis with a Drucker-Prager constitutive model.

corner, as shown by the inset figure in Figure 9 (i). The purpose of this demonstration example is twofold: (i) to demonstrate the NURBS plasticity framework on a non-standard yield function and (ii) to validate its use in three-dimensional analysis. Although this is a simple problem in terms of geometry and boundary conditions it is a challenging problem for the individual finite element due to the high stress gradient across the material and the highly non-linear nature of the force versus displacement response.

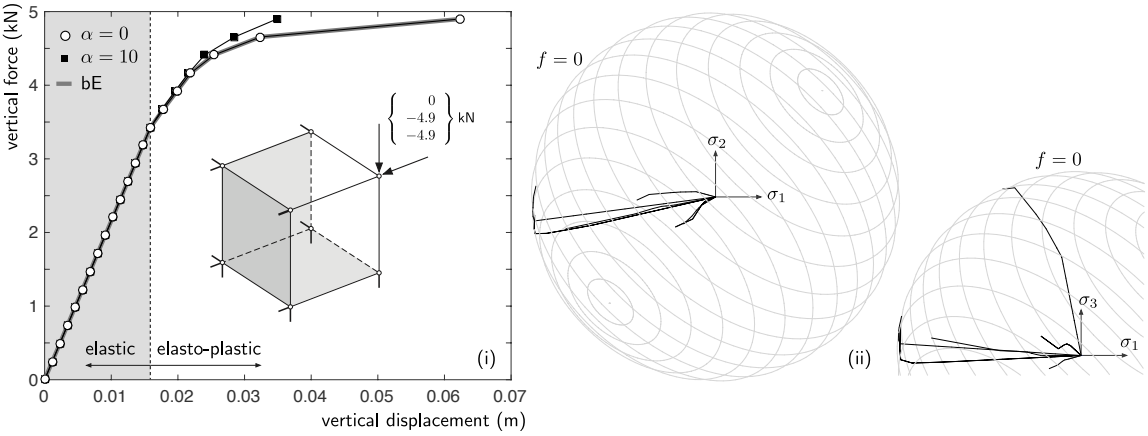

Figure 9: Three-dimensional unit cube: (i) force versus displacement response and (ii) stress paths for perfect plasticity.

The cube was modelled using a single fully-integrated 8-noded hexahedral element with

a Young's modulus and Poisson's ratio of $E = 1$MPa and $\nu = 0.2$, respectively. Yielding of the material was governed by a spherical yield surface

$$f = ||\sigma_i|| - h\sigma_y = 0, \tag{37}$$

where $\sigma_y = 20$kPa and the evolution of h was controlled through (9). The yield envelope was represented using a bi-quadratic NURBS surface (a circle in the two local directions), as shown in Figure 9 (ii).

A load of 4.9kN was applied to the unconstrained corner in both the negative y and z directions over 20 equal loadsteps and the force versus displacement response for both perfect plasticity ($\alpha = 0$) and isotropic hardening (with $\alpha = 10$) are shown in Figure 9 (i). In both cases the first 13 loadsteps are elastic (the grey shaded region in Figure 9 (i)) and the responses of the two models are identical. As expected the hardening material has a stiffer post-yield response due to the expansion of the yield surface with inelastic straining.

Figure 9 (ii) shows the stress paths of the eight Gauss points through the simulation. The spherical yield surface is shown by the light grey lines whereas the stress paths are solid black lines. The stress paths are shown in two views, one showing the whole yield surface aligned with the σ_1-σ_2 plane and the other showing part of the yield surface aligned with the σ_1-σ_3 plane. The stress paths are linear until the first Gauss point reaches yield. The stress path of the Gauss point reaching the yield envelop is obviously constrained to lie on the yield surface but this also causes changes in the direction of the stress paths of the other Gauss points due to stress redistribution within the cube.

Table 3 gives the global normalised residual out of balance force in the case of perfect plasticity for each of the global Newton iterations for loadsteps 16 through 20. The tolerance on the residual was set to 1×10^{-9} and the maximum number of iterations within any loadstep was 5. The final iteration within each loadstep demonstrates quadratic (or near quadratic when hampered by machine precision) convergence indicating the correct implementation of the algorithmic tangent. The convergence of the hardening yield surface follows a similar pattern with a maximum number of iterations within a loadstep of 5. The total number of iterations over the 20 loadsteps was the same as the perfect plasticity case at 38.

The analysis was also conducted with a conventional perfect plasticity bE implementation of the spherical yield surface. As expected, the global force displacement response was identical to the NURBS model, as shown by the thick solid grey line in Figure 9 (i), and the total number of iterations was also 38. However, the bespoke bE algorithm was faster than the NURBS model with a average run time per iteration of 6.9×10^{-3}s compared to 18.5×10^{-3}s for the NURBS implementation. The major cost of the NURBS algorithm is the repeated calculation of the basis functions and their derivatives at each iteration within the plasticity model. This cost can be reduced by reducing the number of control points used to define the surface through only defining the yield surface over the one sextant of principal stress space where $\sigma_1 \geq \sigma_2 \geq \sigma_3$. In this case the number of control points was

reduced from 45 to 15 and the run time per iteration to 16.1×10^{-3}s.

	loadstep				
NR iteration	16	17	18	19	20
1	2.47×10^{-4}	1.68×10^{-4}	1.53×10^{-2}	5.92×10^{-3}	5.43×10^{-2}
2	2.91×10^{-8}	1.08×10^{-8}	4.08×10^{-4}	4.54×10^{-5}	2.35×10^{-2}
3	1.08×10^{-15}	4.24×10^{-16}	1.78×10^{-7}	3.04×10^{-9}	1.75×10^{-3}
4	-	-	6.50×10^{-14}	8.56×10^{-16}	9.02×10^{-6}
5	-	-	-	-	2.68×10^{-10}

Table 3: Three-dimensional unit cube convergence for perfect plasticity ($\alpha = 0$).

5. Conclusions

This paper has extended the work of Coombs *et al.* [8] on NURBS-based isotropic perfect plasticity to include isotropic hardening. The proposed framework allows any smooth isotropic yield envelope to the represented an evolve with inelastic straining. The implicit backward Euler stress integration contains three unknowns, the local knot position on the surface, (ξ, η) and the hardening parameter, h, and enforces the consistency conditions throughout the stress return path and not just at the updated stress state. This results in an efficient (only iteratively inverting a three by three system) and stable (remaining on the yield surface) algorithm that converges at the correct asymptotic quadratic rate. Although this stress integration approach is unlikely to be as efficient as a bespoke constitutive model for a specific yield surface, the impact of the efficiency of the constitutive model on the overall run time of a finite element simulation reduces as the analysis size increases due to more time being spent in the linear solution as compared to the integration of stiffness and internal force. The efficiency of the NURBS plasticity approach can also be increased through the reduction of the number of control points by only defining the yield envelope over the $\sigma_1 \geq \sigma_2 \geq \sigma_3$ portion of stress space. The algorithm also allows for the derivation of the algorithmic consistent tangent that ensures optimum convergence of the global equilibrium iterations. The framework has been demonstrated on both pressure insensitive (von Mises) and sensitive (Drucker-Prager and a sphere) yield surfaces under the conditions of perfect plasticity, hardening and softening for plane stress, plane strain and three-dimensional problems. Where possible the models have been validated against published results and the errors in the stress return algorithm, both in terms of the updated stress path and the hardening parameter, quantified.

The key advantage of the proposed formulation is that it allows any smooth isotropic yield surface to be modelled by only changing the control point information and does not require any modification to the implemented code.

References

[1] R. de Borst, The zero-normal-stress condition in plane-stress and shell elastoplasticity, Communications in Applied Numerical Methods 7 (1991) 29–33.

[2] J. Clausen, L. Damkilde, L. Andersen, An efficient return algorithm for non-associated plasticity with linear yield criteria in principal stress space, Computers & Structures 85 (2007) 1795–1807.

[3] W.M. Coombs, Finite deformation of particulate geomaterials: frictional and anisotropic Critical State elasto-plasticity, Ph.D. thesis, Durham University, 2011.

[4] W.M. Coombs, R.S. Crouch, Algorithmic issues for three-invariant hyperplastic critical state models, Comput. Methods Appl. Mech. Engrg. 200 (2011) 2297–2318.

[5] W.M. Coombs, R.S. Crouch, Non-associated reuleaux plasticity: analytical stress integration and consistent tangent for finite deformation mechanics, Comput. Methods Appl. Mech. Engrg. 200 (2011) 1021–1037.

[6] W.M. Coombs, R.S. Crouch, C.E. Augarde, Reuleaux plasticity: analytical backward Euler stress integration and consistent tangent, Comput. Methods Appl. Mech. Engrg. 199 (2010) 1733–1743.

[7] W.M. Coombs, R.S. Crouch, C.E. Heaney, Observations on Mohr-Coulomb plasticity under plane strain, Journal of Engineering Mechanics 139 (2013) 1218–1228.

[8] W.M. Coombs, O.A. Petit, Y. Ghaffari Motlagh, NURBS plasticity: Yield surface representation and implicit stress integration for isotropic inelasticity, Computer Methods in Applied Mechanics and Engineering 304 (2016) 342 – 358.

[9] M. Crisfield, Non-linear Finite Element Analysis of Solids and Structures. Volume 1: Essentials, John Wiley & Sons Ltd, 1991.

[10] R.S. Crouch, H. Askes, T. Li, Analytical CPP in energy-mapped stress space: application to a modified Drucker-Prager yield surface, Comput. Methods Appl. Mech. Engrg. 198 (2009) 853–859.

[11] D. Drucker, W. Prager, Soil mechanics and plastic analysis or limit design, Quart. Appl. Math 10 (1952) 157–164.

[12] A.A. Ilyushin, Some problems in the theory of plastic deformation, Prikl. Mat. Mekh. (1943) 245–272.

[13] M. Kojić, Stress integration procedures for inelastic material models within the finite element method, Appl. Mech. Rev. 55 (2002) 389–414.

[14] A. Kossa, L. Szabó, Exact integration of the von Mises elastoplasticity model with combined linear isotropic-kinematic hardening, International Journal of Plasticity 25 (2009) 1083–1106.

[15] A. Kossa, L. Szabó, Numerical implementation of a novel accurate stress integration scheme of the von mises elastoplasticity model with combined linear hardening, Finite Elements in Analysis and Design 46 (2010) 391–400.

[16] R.D. Krieg, D.B. Krieg, Accuracies of numerical solution methods for the elastic-perfactly plastic model, Journal of Pressure Vessel Technology 99 (1977) 510–515.

[17] B. Loret, J. Prévost, Accurate numerical solutions for drucker-prager elastic plastic models, Comput. Methods Appl. Mech. Engrg. 54 (1986) 259–277.

[18] A. Mendelson, Plasticity: theory and application, The Macmillan Co., NY, 1968.

[19] J.C. Nagtegaal, D.M. Parks, J.R. Rice, On numerically accurate finite element solutions in the fully plastic range, Comp. Meth. Appl. Mech. Engng. 4 (1974) 153–177.

[20] G.C. Nayak, O.C. Zienkewicz, Elasto-plastic stress analysis. a generalization for various constitutive relations including strain softening, Int. J. Numer. Meth. Eng. 5 (1972) 113–135.

[21] L. Piegl, W. Tiller, The NURBS book, Springer Science & Business Media, 2012.

[22] J.C. Simo, Associative coupled thermoplasticity at finite strains: Formulation, numerical analysis and implementation, Comput. Meth. Appl. Mech. Eng. 98 (1992) 41–104.

[23] J.C. Simo, T.J.R. Hughes, Computational inelasticity, Springer, New York, 1998.

[24] J.C. Simo, M.S. Rifai, A class of mixed assumed strain methods and the method of incompatible modes, Int. J. Numer. Meth. Engng. 29 (1990) 1595–1638.

[25] J.C. Simo, R.L. Taylor, Consistent tangent operators for rate-independent elastoplasticity, Comput. Meth. Appl. Mech. Eng. 48 (1985) 101–118.

[26] E.A. de Souza Neto, D. Perić, M. Dutko, D.R.J. Owen, Design of simple low order finite elements for large strain analysis of nearly incompressible solids, Int. J. Solids Struct. 33 (1996) 3277–3296.

[27] E.A. de Souza Neto, D. Perić, D.R.J. Owen, Computational methods for plasticity: Theory and applications, John Wiley & Sons Ltd, 2008.

[28] L. Szabó, A semi-analytical integration method for J2 flow theory of plasticity with linear isotropic hardening, Comput. Meth. Appl. Mech. Engrg. 198 (2009) 2151–2166.

[29] L. Szabó, A. Kossa, A new exact integration method for the DruckerPrager elasto-plastic model with linear isotropic hardening, In. J. Solids Struct. 49 (2012) 170–190.

[30] M. Vrh, M. Halilovič, B. Štok, Improved explicit integration in plasticity, Int. J. Numer. Meth. Engng. 81 (2010) 910–938.

[31] Z. Wei, D. Perić, D.R.J. Owen, Consistent linearization for the exact stress update of prandtl-reuss non-hardening elastoplastic models, Int. J. Numer. Meth. Engng. 39 (1996) 1219–1235.

[32] M.L. Wilkins, Calculation of elastic-plastic flow, Technical Report, California Univ Livermore Radiation Lab, 1964.

[33] M.h. Yu, Advances in strength theories for materials under complex stress state in the 20th century, Appl. Mech. Rev. 55 (2002) 169–218.

Appendix A. Stress transformation

The following relations can be used to transform between six-component and principal stress and strain space

$$\{\hat{\sigma}\} = [Q]^T \left\{ \begin{array}{c} \{\sigma\} \\ \{0\} \end{array} \right\}, \qquad \{\hat{\varepsilon}\} = [Q]^{-1} \left\{ \begin{array}{c} \{\varepsilon\} \\ \{0\} \end{array} \right\} \qquad \text{and} \qquad [\hat{D}] = [Q]^T [D][Q], \quad \text{(A.1)}$$

where $(\hat{\cdot})$ denotes the six-component stress and strain quantities. The transformation matrix is given by

$$[Q] = \left[\begin{array}{cccccc} (q_1)^2 & (q_2)^2 & (q_3)^2 & q_1 q_2 & q_2 q_3 & q_3 q_1 \\ (q_4)^2 & (q_5)^2 & (q_6)^2 & q_4 q_5 & q_5 q_6 & q_6 q_4 \\ (q_7)^2 & (q_8)^2 & (q_9)^2 & q_7 q_8 & q_8 q_9 & q_9 q_7 \\ 2q_1 q_4 & 2q_2 q_5 & 2q_3 q_6 & q_1 q_5 + q_4 q_2 & q_2 q_6 + q_5 q_3 & q_3 q_4 + q_6 q_1 \\ 2q_4 q_7 & 2q_5 q_8 & 2q_6 q_9 & q_4 q_8 + q_7 q_5 & q_5 q_9 + q_8 q_6 & q_6 q_7 + q_9 q_4 \\ 2q_7 q_1 & 2q_8 q_2 & 2q_9 q_3 & q_7 q_2 + q_1 q_8 & q_8 q_3 + q_2 q_9 & q_9 q_1 + q_3 q_7 \end{array} \right], \quad \text{(A.2)}$$

where the components q_i are associated with the trial elastic strain eigenvectors

$$[q] = \left[\begin{array}{ccc} q_1 & q_4 & q_7 \\ q_2 & q_5 & q_8 \\ q_3 & q_6 & q_9 \end{array} \right]. \quad \text{(A.3)}$$

Appendix B. Jacobian matrix

The components of the Jacobian matrix, $[\partial r/\partial x]$, required for the backward Euler stress integration algorithm are

$$\frac{\partial r_1}{\partial \xi} = -(S_{,\xi})_i (S_{,\xi})_i + (\varsigma_i^t - \varsigma_i^n)(S_{,\xi\xi})_i, \tag{B.1}$$

$$\frac{\partial r_1}{\partial \eta} = -(S_{,\eta})_i (S_{,\xi})_i + (\varsigma_i^t - \varsigma_i^n)(S_{,\xi\eta})_i, \tag{B.2}$$

$$\frac{\partial r_1}{\partial h} = -(S_{,h})_i (S_{,\xi})_i + (\varsigma_i^t - \varsigma_i^n)(S_{,\xi h})_i, \tag{B.3}$$

$$\frac{\partial r_2}{\partial \xi} = -(S_{,\xi})_i (S_{,\eta})_i + (\varsigma_i^t - \varsigma_i^n)(S_{,\eta\xi})_i, \tag{B.4}$$

$$\frac{\partial r_2}{\partial \eta} = -(S_{,\eta})_i (S_{,\eta})_i + (\varsigma_i^t - \varsigma_i^n)(S_{,\eta\eta})_i, \tag{B.5}$$

$$\frac{\partial r_2}{\partial h} = -(S_{,h})_i (S_{,\eta})_i + (\varsigma_i^t - \varsigma_i^n)(S_{,\eta h})_i, \tag{B.6}$$

$$\frac{\partial r_3}{\partial \xi} = -\tilde{h}_{,||\Delta\varepsilon_i^{\mathrm{p}}||} \, ||\Delta\varepsilon^{\mathrm{p}}||_{,\xi}\,, \tag{B.7}$$

$$\frac{\partial r_3}{\partial \eta} = -\tilde{h}_{,||\Delta\varepsilon_i^{\mathrm{p}}||} \, ||\Delta\varepsilon^{\mathrm{p}}||_{,\eta} \qquad \text{and} \tag{B.8}$$

$$\frac{\partial r_3}{\partial h} = 1 - \tilde{h}_{,||\Delta\varepsilon_i^{\mathrm{p}}||} \, ||\Delta\varepsilon^{\mathrm{p}}||_{,h}\,. \tag{B.9}$$

See Piegl and Tiller [21] for efficient methods of calculating the first and second derivatives of the NURBS surface, S_i. The derivatives with respect to the hardening function are given by

$$(S_{,h})_i = RC_p^0, \qquad (S_{,\xi h})_i = R_{,\xi}\, C_p^0, \qquad \text{and} \qquad (S_{,\eta h})_i = R_{,\eta}\, C_p^0 \tag{B.10}$$

where the derivative of the plastic strain increment with respect to h is

$$(\Delta\varepsilon^{\mathrm{p}}{}_{,h})_i = -C_{ij}^{\mathrm{e}} T_{jk}^{-1} (RC_p^0)_k. \tag{B.11}$$

The derivatives of the plastic strain increment with respect to ξ and η are

$$(\Delta\varepsilon^{\mathrm{p}}{}_{,\xi})_i = -C_{ij}^{\mathrm{e}} T_{jk}^{-1} (S_{,\xi})_k \qquad \text{and} \qquad (\Delta\varepsilon^{\mathrm{p}}{}_{,\eta})_i = -C_{ij}^{\mathrm{e}} T_{jk}^{-1} (S_{,\eta})_k. \tag{B.12}$$

The derivative of the hardening function with respect to the L^2 norm of the plastic strain increment is

$$\frac{\partial \tilde{h}}{\partial ||\Delta\varepsilon_i^{\mathrm{p}}||} = \alpha \frac{\Delta\varepsilon_i^{\mathrm{p}}}{||\Delta\varepsilon^{\mathrm{p}}||} \tag{B.13}$$

Note the relative magnitudes of the residuals in (17), with the first two residuals will be of the order of stress squared and the third close to unity. Normalising the first two residuals (and the appropriate entries in the Jacobian matrix) with respect to Young's modulus reduces the potential for ill conditioning of the Jacobian matrix.